Communications Earth & Environment https://doi.org/10.1038/s43247-026-03247-y

Article in Press

El Niño–Southern Oscillation strengthened by North Atlantic Iceberg discharge during Heinrich stadial 1

Received: 11 April 2025

Accepted: 21 January 2026

Cite this article as: Yseki, M., Turcq, B., Gutiérrez, D. *et al.* El Niño–Southern Oscillation strengthened by North Atlantic Iceberg discharge during Heinrich stadial 1. *Commun Earth Environ* (2026). https://doi.org/10.1038/s43247-026-03247-y

Marco Yseki, Bruno Turcq, Dimitri Gutiérrez, Renato Salvatteci, Dante Espinoza-Morriberón, Hugues Boucher, Philippe Martinez & Matthieu Carré

El Niño–Southern Oscillation strengthened by North Atlantic Iceberg Discharge during Heinrich stadial 1

Marco Yseki[1a*], Bruno Turcq[1], Dimitri Gutiérrez[2,3], Renato Salvatteci[4], Dante Espinoza-Morriberón[2,5], Hugues Boucher[1], Philippe Martinez[6] & Matthieu Carré[1,7a]

[1] LOCEAN-IPSL, Laboratoire d'Océanographie et du Climat: Expérimentation et Approches Numériques, IRD/Sorbonne Université/CNRS/MNHN, Paris, France

[2] Instituto del Mar del Peru (IMARPE), Esquina General Gamarra y Valle, Callao, Peru

[3] Laboratorio de Ciencias del Mar, Facultad de Ciencias y Filosofía, Universidad Peruana Cayetano Heredia, Lima, Peru

[4] Center for Ocean and Society, Kiel University, Kiel, Germany

[5] Facultad de Ingeniería, Universidad Tecnológica del Perú, Jirón Hernán Velarde 260, Cercado de Lima, Lima, Perú

[6] UMR 5805 EPOC, Université de Bordeaux-CNRS-EPHE. Pessac Cedex. France

[7] Universidad Peruana Cayetano Heredia, Facultad de Ciencias y Filosofia, Centro de Investigación para el Desarrollo Integral y Sostenible, Laboratorios de Investigación y Desarrollo, Lima, Peru.

* Corresponding author: Marco Yseki (marco.yseki@gmail.com)

[a] These authors contributed equally to this work

Abstract

The last deglaciation provides an opportunity to assess the response of El Niño–Southern Oscillation to rapid warming and disruptions of the Atlantic Meridional Overturning Circulation, both projected in the near future. We present a reconstruction of deglacial El Niño–Southern Oscillation activity using finely laminated sediments from the El Niño–Southern Oscillation-sensitive Peruvian margin. An interannual record of titanium fluxes, a proxy for riverine discharge, shows that the frequency of extreme Eastern Pacific El Niño events and the amplitude of El Niño–Southern Oscillation variability were higher during the deglaciation and peaked during episodes of massive iceberg discharge into the North Atlantic. Maximum El Niño–Southern Oscillation variability occurred in the early phase of Heinrich event 1, at ~17.3–16.7 kyr BP, associated with at least five extreme floods per century in southern Peru. This proxy evidence linking El Niño–Southern Oscillation and the North Atlantic suggests a possible increase in El Niño-related extreme climatic events under future Atlantic Meridional Overturning Circulation weakening.

Introduction

El Niño-Southern Oscillation (ENSO), the most energetic mode of global interannual climate variability, is a source of extreme and potentially catastrophic climatic events, especially in South America[1–3], but its future behavior is still highly uncertain[4–6]. In particular, the response of ENSO and of the tropical Pacific circulation to the weakening of the Atlantic Meridional Overturning Circulation (AMOC)[7,8] is a pressing and debated issue that has traditionally been explored using numeric experiments simulating AMOC reduction events[4,9,10].

Here, we study the links between ENSO and the North Atlantic using proxy observations of ENSO variability (hereafter defined as the standard deviation of the interannual frequency band) during the last deglaciation, *ca*. 18 to 11 thousand years ago (ka), a period of abrupt global warming

associated with a ~80 ppm increase in atmospheric CO_2[11]. At the beginning of the deglaciation, ~18 to 14.5 ka, a destabilization of the northern ice sheet produced a massive discharge of icebergs into the North Atlantic[12–14], an event known as Heinrich Event 1 (H1), followed by a rapid melting of polar ice sheets and sea level rise[15,16]. The freshwater released by iceberg melting in the North Atlantic triggered a substantial slowdown of the AMOC[17,18] with strong global impacts including a cooling (warming) of the northern (southern) hemisphere, and an abrupt perturbation of monsoon systems[19,20]. Climate model "hosing" experiments mimicking this freshwater discharge consistently reproduce the AMOC shutdown and the interhemispheric temperature change, but the response of the tropical Pacific appears model dependent[9,10,21,22]. On the other hand, proxy observations of ENSO during the last deglacial warming are still scarce. In the Eastern Equatorial Pacific (EEP), individual foraminifera analyses (IFA) using subsurface-dwelling species suggested a 16 to 60% increase in ENSO variability in three deglacial snapshots (12.5, 15.1 and 17.9 ka)[23], while no increase was found at 16.8 ka using surface-dwelling foraminifera species[24] also influenced by seasonality changes[25]. Recently, three new foraminifera-derived snapshot records from the EEP found increased ENSO variability at 14.9 ka, during H1, and decreased at 12.3 ka (Younger Dryas) and at 13.4 ka (Bølling-Allerød), suggesting that the mean climate state may modulate ENSO's response to freshwater flux[26]. However, distinguishing a forced response of ENSO from its very large internal centennial variability requires long high-resolution time series. Long, unforced equilibrium GCM simulations suggest that a period of 500 years may be necessary to obtain a statistically robust estimate of ENSO variability[27], while Holocene transient simulations indicate that the centennial-scale unforced variability of ENSO is comparable in magnitude to orbitally forced changes[28]. An initial attempt to reconstruct long-term ENSO activity from lithic flux on the Peruvian margin, using photoreflectance, did not yield the required interannual-scale resolution during H1[29]. Here, we present a continuous multimillennial sedimentary record of

ENSO activity, derived from interannually resolved XRF measurements, extending back into H1 to assess ENSO's response to planetary warming and AMOC disruption.

The core M77/2-005-3 (12º05 S, 77º40,07 W) was collected off Callao at 214 m depth, and core G14 (14.38ºS, 76.42ºW) was collected off Pisco at 390 m depth on the Peruvian margin (Fig. 1, Methods). We focus here on sections of the last deglaciation (18–13 ka) from both cores and a Late Holocene section (2.7–1.3 ka) from Callao, which show irregularly spaced but well-preserved laminae indicating minimal sediment mixing (Methods, supplementary Figs. 1–4), allowing analysis of high-frequency variability.

Clays in marine sediment of the continental margin are mostly of riverine origin[30–32] and enriched in titanium (Ti)[33,34], which makes this element a reliable tracer of fluvial sediment input in central Peru (Methods), as it has been in other similar geographical settings[35–37]. XRF Ti counts, normalized (Ti_{norm}) to account for matrix variability effects, is therefore a tracer of rainfall in the multiple watersheds extending from the altiplano to the arid Pacific coast and strongly connected to ENSO (Fig. 1).

Results and discussion

The regional climatic significance of the records is demonstrated by the covariance between sedimentary records off Pisco and Callao, previously shown by multiple organic and inorganic tracers in box cores collected at the same sites[32,38]. It is observed here on a longer timescale, not only in Ti_{norm} variations but also in the millennial changes of interannual variability (Fig. 2).

Compared to the 1400-year-long Late Holocene section of the Callao core, Ti_{norm} values are on average ~30% higher during the deglacial period (Fig. 2a). Lower sea level might be partly responsible for the higher Ti content because of the reduced distance to the river mouths: the coast at Callao was ~20 km closer to the coring site at 18 ka, but not significantly closer at Pisco due to

the abruptness of the inner shelf (Fig. 1b). However, sea level rose strongly from 18 to 13 kyr BP, a trend that is not reflected in the Ti_{norm} record at either Callao or Pisco. Hence, the larger deglacial Ti_{norm} values likely result from increased river discharge in central-southern Peru. Since coastal precipitation is rare and mostly occurs at this latitude during extreme Eastern Pacific (EP) El Niño events (Supplementary material), the larger average river flow was primarily caused by strengthened South American monsoon in the Andes and their foreland, in agreement with records of increased precipitation in the northern and central Andes[37,39,40] and with evidence of a southern shift of the ITCZ mean position at that time[41].

A high-resolution sediment record of ENSO variability

During EP El Niño events[42], the most extreme warming is observed along the Peruvian coast (anomalies up to 8 °C), making it one of the regions most sensitive to ENSO[43] (Fig. 1a). Because these warm waters trigger atmospheric convection and thunderstorms along this typically hyperarid coast[1,2], precipitation in the Peruvian coastal lowlands is significantly correlated with the eastern Pacific E index[3,44] (Fig. 1d). During extreme events such as 1997–1998, the steep and usually dry valleys that drain the western flank of the Andes (Fig. 1b) are suddenly activated, producing mud floods on both the northern and southern coasts[45] (Supplementary text and supplementary Fig. 6). Anomalous clastic flux in marine sediments and debris flow deposits in lower valleys have yielded a consistent chronology of extreme events in the Holocene in the northern, central and southern coast[46–49]. Apart from these extraordinary events, the fluvial sediment discharge depends on rainfall on the Altiplano, which, on interannual timescale, is primarily determined by ENSO conditions in the central equatorial Pacific [3,50–52] (Fig. 1c). We therefore extract two independent metrics from the Ti_{norm} record: 1) the relative standard deviation (RSD) of the 2.5–8 yr ENSO frequency band associated with the impact of Central Pacific (CP)

ENSO in the Andes, and 2) the frequency of extreme events associated with the impact of extreme EP El Niño events on the southern coast (Methods).

ENSO-related RSD appears higher in Callao than in Pisco (Fig. 2c), likely due to closer river mouths and stronger ENSO anomalies toward lower latitudes (Supplementary Fig. 6). Yet, ENSO RSD variations are largely coherent in both sites reflecting ENSO variability modulations in the central Pacific. Three maxima are observed in both sites in CP ENSO variability *ca*. 13.5–13.8 ka, 15.4–15.9 ka, and 16.7–17 ka, with different relative amplitudes, the earliest peak being the highest in both cores. Differences between the sites also include offsets in the timing of ENSO changes, in particular with the start of the first peak. These differences are likely due to dating uncertainty, uncertainty in the temporal resolution, and to different coastal morphological evolution across the deglaciation that affect sediment transport and deposition. Uncertainties in Ti_{norm} as a proxy for ENSO activity on the Peruvian margin also arise from the contribution of aeolian sediments from the arid coast, from atmospheric teleconnections with other regions and modes of variability. We minimize the potentially confounding effect of aeolian flux by using independent metrics specific to ENSO coastal and Andean teleconnections (Methods, Supplementary Figs. 8,9). Primary productivity has a diluting effect on Ti_{norm} that tends to amplify the signal of extreme EP events, since productivity is negatively linked to EP ENSO variability[53]. We therefore discuss below the changes observed in the mean climate, CP ENSO variability, and the frequency of extreme EP El Niño events during the deglacial warming.

ENSO variability during the deglaciation

Changes in CP ENSO variability (measured here as a relative standard deviation in 300-yr moving windows, see methods) during the deglacial climate ranged approximately from -10% to +105% compared to the Late Holocene (Fig. 2c), when ENSO had similar to modern

characteristics[23,24,28,49,54,55]. ENSO is known to be subject to large decadal to centennial internal unforced modulations[27,28,56] but the duration of this record allows a robust measurement of variability ranging from similar to substantially higher during the deglaciation, especially during H1 (~18–15 ka), in broad agreement with foraminifera-based estimates[23,26] (Fig. 3d,e,f). Within the deglaciation, the interannual-to-multidecadal frequency bands exhibit similar millennial-scale variation patterns, consistent with the well documented relationship between the Pacific decadal variability and ENSO[57]. However, whereas interannual variability was larger during H1 compared to the Late Holocene, the decadal and multidecadal variability were substantially weaker (Supplementary Fig. 7), indicating conditions that favored ENSO variability in the Pacific relative to lower frequency bands.

Large millennial-scale changes are observed within the deglaciation, both in the frequency of extreme EP events and in CP ENSO variability (Fig. 3). The reproducibility of these independent metrics (Supplementary Fig. 8) and the 4500-year time span of the record provides exceptional statistical robustness for this ENSO reconstruction. The covariance of these complementary metrics indicates a qualitatively similar response of ENSO in the central and eastern Pacific.

Relationship with the ITCZ and South American monsoon

Weakening events of the AMOC have been shown to produce southern shifts of the ITCZ[41,58]. Could the deglacial ENSO peaks recorded in Peru result from these ITCZ shifts? Two lines of evidence suggest otherwise. First, the mean position of the ITCZ may affect remote ENSO atmospheric teleconnections with the tropical Andes and could therefore modulate our record of interannual variability, but it would not directly influence the ENSO-precipitation relationship in the Peruvian coast. Since precipitation anomalies on the Peruvian coast during extreme EP events are triggered by the atmospheric convection occurring locally over nearby anomalously warm

waters[3], the record of EP extreme events is not modulated by the mean ITCZ position or the South American monsoon strength. Second, peaks of ENSO variability are not associated with Ti_{norm} maxima that would characterize phases of strengthened monsoon. We conclude that centennial-scale modulations of ENSO variability in our record are not caused by ITCZ or monsoon changes. On the other hand, the high frequency of extreme EP El Niño events recorded during H1 must have had profound impacts on the hydrology and ecosystems of South America.

Links of ENSO with the North Atlantic during H1

Heinrich event 1 (H1) was a period of destabilization of the Laurentide and Eurasian ice sheets resulting in massive discharge of icebergs drifting into the North Atlantic[12,14,59,60]. The fresh and cool water released over a vast surface area blocked the formation of North Atlantic deep water, leading to the substantial slowdown of the AMOC. This circulation change reduced northward heat transport, leading to strong cooling in the North Atlantic and warming in the South Atlantic, an interhemispheric seesaw that extended to the Pacific basin[10,21,22,61–64].

Detailed records of ice-rafted debris (IRD) showed that H1 includes two main events of iceberg discharge, the first one being the largest[13,14]. Here we compare ENSO deglacial modulations with high resolution IRD records from the Nordic sea that track centennial-scale variability of freshwater forcing in the area of Atlantic deep water formation[59,65] (Fig. 3c). Two large peaks are also observed in CP ENSO variability (Fig. 3d) and EP extreme event frequency (Fig. 3e) within H1. The first peak of ENSO, dated at ~17.3–16.7 ka represents a doubling of CP ENSO variability compared to the Holocene. A maximum frequency of 6 extreme EP events per century is observed while it is less than 1 per century after H1 or in Late Holocene coastal flood deposits[46]. A second peak, dated at ~16–15.3 ka, represents a ~50% increase in CP ENSO variability and 2–3 extreme events per century. Including secondary peaks, a total of six maxima of ENSO activity are detected

in the eastern Pacific, coinciding with the timing of IRD peaks within the limits of dating uncertainty (Fig. 3).

The effects of an AMOC shutdown have been explored in coupled global climate models (CGCMs) by applying a strong, transient freshwater forcing to the North Atlantic[58]. CMIP3 models mostly find an amplification of ENSO variability associated with zonally more symmetric mean conditions and a reduced annual cycle[21,62–64], and has been generally explained by the non-linear frequency entrainment theory[21,66]. While simulations are consistent with the strong reduction of the zonal and cross-equatorial SST gradients during H1 shown by SST reconstructions[23,67] (Fig. 3g), the negative ENSO-annual cycle link proposed by the frequency entrainment hypothesis is, however, not supported by seasonally resolved proxy observations[28,68]. ENSO spatial pattern has also been found to be sensitive to North Atlantic freshwater forcing in CGCMs, exhibiting an eastward shift of ENSO variance in a perturbed control experiment[22] and in an early Holocene configuration[69], but a shift toward more central Pacific activity under an anthropogenic climate change scenario[10]. A recent modelling study proposed that a collapse of the AMOC could reduce ENSO activity by strengthening the Walker circulation[9], which is opposite to proxy observations. Our results, together with previous foraminifera-based estimates[23,26], support an intensification of both the E and C modes of ENSO in response to North Atlantic freshwater forcing. These changes in ENSO arise from a shift in the background state of the tropical Pacific. Proxy observations indicate reduced rainfall in the northern tropics and increased rainfall in the southern tropics during H1, consistent with the southern shift of the mean ITCZ position simulated in most climate model hosing experiments[58,62,70,71]. Analysis of modeling experiments consistent with observations indicate a transmission of the Tropical North Atlantic cooling to the Pacific basin through cooler trade winds across the Central American Isthmus[71]. The cooling of the northeastern tropical Pacific reduces the meridional temperature gradient, increasing rainfall in the southeastern tropical Pacific

and the Andes, and leads to a weakening of the zonal temperature gradient. Our record supports a mechanistic link with iceberg discharge events through air-sea interaction rather than a marine teleconnection associated with AMOC slowdown[61,64]. Indeed, when AMOC was overall much weaker during H1, centennial-scale variability is not observed[72], as in the ENSO records (Fig. 3), which points to the anomalous SST field in the North Atlantic as the primary driver of ENSO changes during H1 through rapid atmospheric teleconnections.

The mechanisms of ENSO enhancement during H1 is likely related to the reduced zonal and meridional SST gradients in the tropical Pacific, according to CGCMs with the best ENSO representation[4] and according to the strong ENSO-mean state correlation in proxy data[23]. A more zonally and meridionally symmetric SST pattern shifts the westerly wind anomalies that trigger ENSO eastward and facilitates the onset of convection in the eastern Pacific, thereby increasing the likelihood that these anomalies develop into extreme El Niño events[64].

Mixed forcings during the deglaciation

A number of additional rapidly changing forcing factors may have influenced ENSO behavior during the deglaciation, including insolation, the presence of large polar ice sheets, and greenhouse gases. The change in the seasonal flux of solar energy related to the Earth's orbital parameters has been shown to be a significant driver of ENSO in models[68,73,74], and to account for the mid-Holocene ENSO minimum (3–6 kyr BP) in paleoclimate records[28]. While orbital forcing cannot account for multicentennial-scale peaks in ENSO variability during H1 (Fig. 3), its damping effect on ENSO, strengthening towards the precession minimum at 11 ka[28,66,73,75], may have contributed to the long-term decreasing trend observed from 18 to 13 ka (Fig. 3d,e). The orbital damping effect in the Early Holocene climate simulations was found to exceed the strengthening effect of a freshwater flux[75].

The effect of the large ice sheet in the Northern Hemisphere is still unclear. The ice sheet changes the mean position and intensity of the mid-latitude westerly jet stream[66,69], modifying the surface winds in the tropical Pacific, with a model-dependent impact on ENSO variability. In the IPSL-CM4 model, the ice sheet slightly increases ENSO variability in the eastern Pacific[69]. Conversely, in the CCSM3 model TRACE transient simulation of the past 21,000 years (Fig. 3h) forced uniquely by continental ice sheet variations, an abrupt ENSO increase (25%) is found at 14 kyr BP in response to a marked retreat of the Laurentide ice sheet. This effect that disappeared in the all-forcing simulation[66].

How increasing greenhouse gases influence ENSO is also strongly debated. While CMIP5 and CMIP6 model ensembles suggest an increased ENSO variability with increasing atmospheric CO_2 concentrations[76,77], two recent studies found that ENSO is weakening with increasing CO_2 when simulations are run over several millennia[78] or when model biases are minimized with an ultra-high-resolution model[5]. The 80 ppm increase of CO_2 during the deglaciation is slightly lower than the current 100 ppm anthropogenic CO_2 increase that has not yet produced a clearly detectable impact on ENSO, and is much lower than the x2 or x4 scenarios tested for the future that yields contradictory effects[79]. Thus, CO_2 changes could arguably be considered as a relatively minor forcing of ENSO during the deglaciation.

Very few model experiments have, however, explored the combined influence of multiple external forcings on ENSO during the deglaciation. Although TRACE reproduced correctly large-scale features of the evolution of the global climate (e.g., AMOC intensity, cross-Equator SST contrast, tropical Pacific SST), the deglacial reduction of ENSO in the all-forcing experiment is at odds with Peruvian sediments showing increased variability compared to the Late Holocene. Early Holocene meltwater flux experiments also fail to reproduce ENSO variability similar to the modern state[28,69,75]. These disagreements point to an underestimation of ENSO's sensitivity to

iceberg meltwater discharge in these CGCMs, compared to the influence of other forcings. This issue is lekely shared by other climate models and may bias projections.

Implications for future trends

There are multiple lines of evidence for a slowdown of AMOC in the 20th century, possibly as a result of Greenland ice sheet melting[7,80–82], which is accelerating with global warming[83]. CMIP6 models project a sustained weakening of the AMOC during the 21st century[84]. An underestimation of the impact of meltwater discharge and AMOC weakening on tropical climate variability in climate models, as suggested by our results, raises serious concerns in the context of current global warming. However, the AMOC slowdown during H1 bears substantial differences from the modern and potential future weakening. Modern AMOC weakening is thought to result from various forcings, including greenhouse gases, anthropogenic aerosols, and Greenland meltwater[80,81,85]. Meltwater flux would not be spatially distributed by drifting icebergs but would have a more coastal influence, and would therefore be associated with a different pattern of SST anomalies[10,81]. A recent study showed that the AMOC and SST responses to freshwater depends on the region of input[86]. Since evidence converges on identifying the SST field and atmospheric teleconnections as the key drivers of ENSO changes during H1, these differences prevent a simple extrapolation of an analogous ENSO response in the future. Our record provides a benchmark for further transient climate simulations to evaluate the relative response of ENSO to competing forcings in models.

Conclusions

Laminated marine sediments off Peru provide a ~4,500-year-long continuous record of centennial- to millennial-scale changes in CP ENSO variability and in the frequency of extreme EP events

during the deglaciation. The doubling of CP ENSO variability during the first phase of H1 represents the highest level recorded to date, thereby extending the known potential range of such fluctuations. The frequency of extreme EP El Niño events is more than one every 20 years during that period. Millennial-scale peaks of ENSO coincide with the timing of massive iceberg discharge in the North Atlantic. The record provides thus a clear support to climate models that found a strengthening of ENSO in the eastern Pacific in response to freshwater input to the North Atlantic. SST changes associated with the spatial distribution of iceberg meltwater flux in the North Atlantic were likely the primary driver of ENSO changes via atmospheric teleconnections and a relaxation of zonal and meridional SST gradients in the Eastern tropical Pacific. The role of AMOC weakening at that time is less clear: on one hand, it is tightly linked to North Atlantic surface conditions and is assumed to respond rapidly to meltwater flux; on the other hand, its changes appear slower than those of IRD and ENSO during the deglaciation. Although a direct prediction of future El Niño behavior cannot be drawn from these results given the profound differences between H1 climate conditions and those expected in the future (global temperature, ice sheet volume, forcing of AMOC), our record allows the assessment of CGCMs' ability to produce a realistic response of ENSO in a context of mixed forcings and abrupt global change. Overall, our paleoclimate data indicate that iceberg meltwater flux in the North Atlantic was the primary forcing of ENSO variability during the last deglaciation.

METHODS

Marine sediments core

The cores from Callao (M77/2-005-3, 11.08°S, 78.02°W, water depth 210 m) and Pisco (G14, 14.38 °S, 76.42 °W, water 390 m) were retrieved from the southeast Pacific continental slope

during the M77-2 and Galathea-3 expeditions respectively[91,92]. The lithology of both cores, previously described by Salvatteci *et al.*[91,92] is here complemented by X-Ray images and presented in supplementary Fig. 1 and supplementary Fig. 3. The Late Holocene and deglacial sediments are mainly composed of “irregularly spaced laminae” and “isolated laminae”, as defined by Brodie and Kemp[93]. The “irregularly spaced laminae” are packets of laminae (several centimeters to decimeters thick) separated by intervals of homogeneous sediments (several centimeters to decimeters thick). These laminae packages include alternations between diatom oozes and diatomaceous mud, the latter with a higher content of clay minerals. The "isolated laminae" are packets of millimetric and sub-millimetric laminae (solitary diatom ooze) enclosed in homogeneous mud. The Pisco core is more finely laminated than the Callao core. The chronology is based on 26 ^{14}C datings in the Callao core, and 29 ^{14}C datings in the Pisco core, obtained on bulk sediment organic matter (Supplementary Table 1). Radiocarbon dates were calibrated using the Marine20 dataset[94], and a reservoir age deviation $\Delta R=367\pm40$ years estimated for the Late Holocene in southern Peru[91,95,96]. Bayesian age models were calculated with the Bacon R package[97] (Supplementary Fig. 2 and 4). The analyzed section (36–588 cm) of the Callao core included the last deglaciation (17–13 kyr BP; 102–588 cm), and, above a sedimentation hiatus at 94 cm, part of the Late Holocene (2.7–1.4 kyr BP; 36–93 cm). Holocene sediments were not recovered in Pisco, which is common in sediment cores of the region, especially for the mid-Holocene, which has been interpreted as the result of erosion by bottom currents[98,99]. The analyzed section (10–285 cm) of the Pisco core spans the last deglaciation (18–13.5 kyr BP). Depth-age models indicate reasonably constant sediment accumulation rates in the analyzed sections, and were thus estimated by a linear regression. We obtained accumulation rates of 0.7 mm/yr in Pisco, and of 0.5 mm/yr and 1.2 mm/yr in Callao for the Holocene and deglacial sections respectively. In

the deeper parts, the accumulation rate was too low for interannual variability to be estimated from this record.

XRF analysis

Ti was measured at high resolution (1 mm) in both cores using an XRF scanner, but only in the laminated or banded sections of the sediment cores to ensure that the analyzed intervals represent deposition from the water column rather than reworking of upslope material[91]. XRF analyses of the Callao core were performed at the ALYSES facility (IRD-Sorbonne University, Bondy, France) using a Bruker-ARTAX µ-XRF core scanner with a Cr anode and polycapillary X-Ray optics at 25 kV and 500 µA during 10 s. The Pisco core was analyzed at the University of Bordeaux 1 using an Avaatech core scanner at 10 kV and 400 µA during 10 s.

XRF does not only depend on elemental concentrations but also on changes in matrix physical properties such as density, grain size or water content[100,101]. To correct for this matrix effect, Ti counts were normalized (Ti_{norm}) by the 20-yr smoothed sum of all the other elements to correct for low frequency, centimetric scale, changes of the matrix effect. Ca was excluded because of the large variability related to postdepositional calcium carbonate dissolution on the southern Peruvian margin[91]. This approach is similar to the centered log-ratio method but avoids suppressing the short-term positive anomalies associated with extreme El Niño events, which are the focus of this study.

Relationship between Ti and rainfall

Ti in marine sediments is associated with terrestrial particles transported to the ocean either by rivers or by wind. West of the Peru-Chile trench, lithogenic material in marine sediments is primarily composed of aeolian particles eroded from the south-American coast[102]. On the

continental margin, however, the lithogenic fraction is primarily composed of clay transported by rivers and secondarily of a coarser fraction transported by wind[30,32]. Clay particles are enriched in Ti compared to coarser particles because titanium is mainly present as oxides resulting from weathering and pedogenesis, bound to clay minerals[33,34,103–105]. This is supported in Peru by the Ti-enriched clayish layer observed in marine sediment trap following the 2017 flood[106] (supplementary Fig. 5). Because lithogenic sediments are largely composed of river-transported clays enriched in Ti, we interpret Ti as a proxy of fluvial discharge, as in previous studies in similar environments [35–37,107]. This is confirmed by the negative correlation observed between Ti_{norm} mean and Ti_{norm} standard deviation, inconsistent with an aeolian source of Ti, but consistent with the negative impact of CP ENSO on river discharge (Supplementary Fig. 10). The contribution of aeolian sediment, and its temporal variations, does, however, introduce uncertainty in the proxy interpretation. We minimize this issue by using two independent and complementary statistical metrics that characterize CP and EP ENSO rainfall responses (see Fig. 1c,d, and below), isolating the rainfall signal from the wind-derived noise.

ENSO diversity and teleconnection in Peru

El Niño events may be categorized into general types, or flavors, based on the spatial pattern of temperature anomalies, which are associated with distinct atmospheric teleconnection patterns[108]. We briefly review here the impacts on the Peruvian rainfall regime of the Central Pacific (CP), Eastern Pacific (EP)[42], and coastal El Niño events, to decipher how Ti variability relates to ENSO in our study sites.

The impact of Eastern Pacific (EP) El Niño events on Peruvian coastal rainfall has been reported in many studies. Instrumental data show that SST warm anomalies in the easternmost Pacific associated with the strongest EP events cause anomalously high rainfall on the coastal lowlands

and on the Andes Pacific slope often causing mud floods[3,50,52,109,110]. A significant link between coastal rainfall anomalies and the EP index was found (Fig. 1d) using the PISCOp high resolution rainfall dataset of Peru[3,87]. Floods on the south coast of Peru during extreme EP events are a locally notorious phenomena albeit less catastrophic and thus less commented compared to floods of the northern coast. Evidence of these southern floods is found in news reports, administrative reports, or in subsequent geomorphological observation of the debris flow deposits[47]. In particular, report citations and pictures of the catastrophic flood that occurred in the Ica valley (14–14.8°S) during the 1997-98 extreme El Niño event are provided in supplementary material. Precipitation on the coast activates a network of usually dry steep valleys and mobilize a disproportionate amount of sediment turning into mud floods. Such rare events generate short and massive sediment discharge to the ocean producing clayish layers in the marine sediment[106] characterized by outsized peaks in the Ti record, that no other climatic phenomena could produce.

Central Pacific (CP) El Niño events have no significant impact on coastal rainfall in Peru (even the extreme 2015-2016 CP event) because the deep atmospheric convection occurs mostly in the Niño3.4 region. The CP mode of ENSO has, however, a strong remote atmospheric teleconnection with the High Andes, where rainfall decrease (increases) during warm (cold) events [3,51,109,111] (Fig. 1c). As a result, the interannual variability of summer monsoon rainfall in the Peruvian Altiplano has been shown to be primarily determined by ENSO in the central Pacific[50,51,110–112], which is necessarily translated into interannual variability of coastal river flow.

Coastal El Niño events refer here to warm surface anomalies restricted to the easternmost tropical Pacific, off Peru, that produce anomalous rainfall and flood on the Peruvian coast. Only three such events are known with confidence: two of them are quite recent and well-documented (2017 and 2023), and the third occurred in 1925[113]. These events are characterized by warm SST anomalies lasting a few months in austral summer along the Peruvian coast north of 12°S (Lima). On the

southern coast, where the Pisco core is located, SST anomalies were mild or even negative[114] (Supplementary Fig. 6). Floods occurred in Lima (close to the Callao core) during the 2017 and 2023 events but not in the southern coast. Coastal El Niño events do not appear to be disconnected from global ENSO, since in two cases (1925 and 2023) coastal anomalies spread and evolved into the canonical El Niño events of 1926 and 2024[113–116]. Still, these events could account for differences between our two sedimentary records since the Callao core is located at ~11.1°S, in the range of Coastal El Niño, and the Pisco core is located at ~14.4°S, outside the range of coastal El Niño events. However, the overall coherency between interannual variability changes at both sites suggests a minor influence of coastal El Niño events and a primary influence of large-scale events. Finally, the Pisco (G14) sedimentary record was primarily used here to estimate the frequency of extreme El Niño rainfall, because of more continuous lamination, and because this site is less influenced by coastal El Niño events in the instrumental record.

In summary, coastal El Niño events have limited impact on river flux in the southern coast of Peru, while the interannual frequency band is dominated by the remote influence of the ENSO CP mode on the Peruvian Altiplano, and outsized sedimentary discharges are associated with extreme EP El Niño events. The distinct influences of CP and EP ENSO modes on rainfall form the basis for different ENSO metrics.

ENSO metrics

The XRF analyses with 1 mm steps yield a temporal resolution of 0.8 years in the deglacial sections of the Callao core and 2.2 years in the Late Holocene section (2.7–1.3 kyr). The temporal resolution of the XRF record in the deglacial section of the Pisco core is 1.3 years. The Ti_{norm} records were resampled by linear interpolation at 0.5-year resolution in the deglacial and Late Holocene sections so a 2.5–8 years band pass filter could be equally applied to all records to extract the ENSO

frequency band (Fig. 2b). 10–30 years and 30–100 years band pass filters were also applied to extract decadal and multidecadal variability respectively (Supplementary Fig. 7).

As shown in the previous section, the interannual frequency band is primarily related to the CP mode of ENSO in influencing Andean rainfall, whereas the EP mode only impacts the southern coast in rare extreme events. To correct for a potential effect of background monsoon intensity changes, we used the relative standard deviation (RSD) of Ti_{norm} as an estimate of CP ENSO-related interannual climate variability (standard deviation divided by the Ti_{norm} mean value, calculated over moving 300-year windows). The change in ENSO variability in Callao was calculated as a percentage relative to the Late Holocene average value in Callao.

Coastal rainfall events associated with extreme EP El Niño events were identified by peaks in Ti_{norm} interannual variability exceeding 2σ. The number of extreme events was calculated over 300-year moving windows, and the frequency was expressed in events per century.

RSD(Ti_{norm}) was then calculated after removing extreme events from the interannual variability if Ti_{norm}. We obtain thus a metric linked to the Andean influence of the CP mode of ENSO, independent from extreme EP El Niño coastal floods. Excluding extreme events reduced the interannual variability by up to ~20%, but the centennial variations are unchanged (Supplementary Fig. 8). Importantly, the independent metrics of ENSO, RSD and the frequency of extreme events, are strongly correlated which supports the robustness of the approach, and yields information on the two major modes of ENSO.

The similarities between Callao and Pisco records shown in figure 2 shows the regional representativity and the link with large scale ENSO variability. Then, the record from Pisco was selected to represent past ENSO changes in figure 3 for three reasons: (1) the core has more continuous laminations, (2) it is less influenced by coastal Niño events (Supplementary figure 6),

and (3) it is less influenced by deglacial sea-level rise. The complete record of Callao is presented in Supplementary Figure 9.

Limitations and uncertainties

The contribution of aeolian sediment, and its temporal variations, introduces uncertainty in Ti record's interpretation. We minimized this issue by using statistical metrics that characterize ENSO rainfall response (see previous section). Winds off Peru increase during austral winter but are not clearly linked to ENSO activity since winds tend to be stronger during periods of low ENSO activity[117] but have also been observed to maintain a normal or increased intensity during Niño events[118,119]. Focusing on the variability of the ENSO frequency band thus isolates the ENSO signal from the noise produced by wind activity. In addition, we show that the interannual variability of Ti_{norm} is negatively correlated on centennial timescales with its mean value (Supplementary Fig. 10). This is opposite to the effect that a wind-related flux of Ti would have produced, but consistent with a rainfall signal forced by CP ENSO since higher CP ENSO activity tends to reduced rainfall in the high Andes. Finally, short and extreme peaks of Ti_{norm} correspond to sudden, massive sediment input that is better explained by El Niño-related coastal floods than by wind. The strong correlation between the frequency of extreme EP events and changes in the interannual variability rules out significant influence of aeolian transport and of secondary sources of variability due to teleconnections with other regions, and confirms ENSO as the main driver.

Uncertainty in the record of interannual variability arises from uncertainties in the chronology and thus in the estimate of the sedimentation rate. Here, we used a constant sedimentation rate value because of the quasi linear age-depth model relationship in the analysed sections, although small variations in the sedimentation rate are to be expected, affecting the record's temporal resolution. When the temporal resolution is underestimated, higher, more powerful frequencies are obtained

by the band-pass filter, resulting in an overestimation of the interannual variability. The opposite would occur when the sedimentation rate is overestimated. This effect, likely contributes to the differences observed between the Callao and Pisco records. Radiocarbon dating, due to the large radiocarbon reservoir age in this upwelling area[120], yields confidence intervals larger than 500 years in the deglaciation (Supplementary Figs. 2,4), which likely explains the timing difference in the beginning of the first ENSO peak between Pisco and Callao *ca*. 17.4–17ka.

Finally, Ti_{norm} also depends on variations of the primary productivity that dilutes the terrigenous signal. Primary productivity is influenced by EP conditions of ENSO, with anomalously low productivity observed during El Niño conditions in the eastern Pacific because of a deeper nutricline[53,121,122], and higher productivity during La Niña conditions[53]. EP El Niño events are thus associated with a reduced flux of biogenic silica, thereby amplifying the magnitude of flood-related Ti peaks. Although anomalies in the central Pacific have little influence on Peruvian upwelling, an interannual productivity frequency band necessarily interferes to some degree with the interannual variability of the Ti flux in our record.

Acknowledgements

This publication was supported by the IRD-DPF and ANR-15-JCLI-0003-03 BELMONT FORUM PACMEDY. Part of XRF data were obtained on the ALYSES facility (IRD-UPMC) that was supported by grants from Région Ile-de-France. This work is a contribution of the Collaborative Research Project 754 “Climate-Biogeochemistry interactions in the Tropical Ocean” (www.sfb754.de), which is supported by the Deutsche Forschungsgemeinschaft (DFG). We would like to thank the crew and scientists aboard R/V Meteor cruises M77/2 in 2008 and thank Bo Thamdrup, chief scientist of the Galathea-3 expedition (Leg 14), and Bente Lomstein, who

conducted the core sampling onboard the RV Vaedderen. We thank SENAMHI and NOAA for sharing climate datasets.

Data availability

The Ti_{norm} time series and ENSO metrics of sediment cores G14 and M77/2-005-3 are available for reviewers at https://figshare.com/s/e4da7a2aed5d676d6100

The dataset will be made publicly available if and after the article is accepted for publication, with doi:10.6084/m9.figshare.29583158. The PISCOp rainfall dataset is available at https://doi.org/10.6084/m9.figshare.21127423.v2.

Author contributions

MY and MC contributed equally to this work. MY, BT, DG and MC designed the study. MY and MC wrote the manuscript. RS, PM and HB measured XRF data. MY and DEM analyzed data. MY, MC, BT, DG, RS, PM, HB and DEM contributed to the interpretation of the data and the preparation of the final manuscript.

Competing interests

The authors declare no competing interests.

References

1. Garreaud, R. D. The Andes climate and weather. *Advances in Geosciences* **22**, 3–11 (2009).
2. Grimm, A. M. & Tedeschi, R. G. ENSO and extreme rainfall events in South America. *Journal of Climate* **22**, 1589–1609 (2009).
3. Sulca, J., Takahashi, K., Espinoza, J.-C., Vuille, M. & Lavado-Casimiro, W. Impacts of different ENSO flavors and tropical Pacific convection variability (ITCZ, SPCZ) on austral

summer rainfall in South America, with a focus on Peru. *International Journal of Climatology* **38**, 420–435 (2018).

4. Cai, W. *et al.* Changing El Niño–Southern Oscillation in a warming climate. *Nature Reviews Earth & Environment* https://doi.org/10.1038/s43017-021-00199-z (2021) doi:10.1038/s43017-021-00199-z.
5. Wengel, C. *et al.* Future high-resolution El Niño/Southern Oscillation dynamics. *Nature Climate Change* **11**, 758–765 (2021).
6. Seager, R. *et al.* Strengthening tropical Pacific zonal sea surface temperature gradient consistent with rising greenhouse gases. *Nature Climate Change* **9**, 517–522 (2019).
7. Caesar, L., McCarthy, G. D., Thornalley, D. J. R., Cahill, N. & Rahmstorf, S. Current Atlantic Meridional Overturning Circulation weakest in last millennium. *Nature Geoscience* **14**, 118–120 (2021).
8. Masson-Delmotte, V. *et al.* Climate change 2021: the physical science basis. *Contribution of working group I to the sixth assessment report of the intergovernmental panel on climate change* **2**, 2391 (2021).
9. Orihuela-Pinto, B., Santoso, A., England, M. H. & Taschetto, A. S. Reduced ENSO Variability due to a Collapsed Atlantic Meridional Overturning Circulation. *Journal of Climate* **35**, 5307–5320 (2022).
10. Liu, W., Duarte Cavalcante Pinto, D., Fedorov, A. & Zhu, J. The Impacts of a Weakened Atlantic Meridional Overturning Circulation on ENSO in a Warmer Climate. *Geophysical Research Letters* **50**, e2023GL103025 (2023).
11. Marcott, S. A. *et al.* Centennial-scale changes in the global carbon cycle during the last deglaciation. *Nature* **514**, 616–619 (2014).

12. Bond, G. *et al.* Evidence for massive discharges of icebergs into the North Atlantic ocean during the last glacial period. *Nature* **360**, 245–249 (1992).

13. Hodell, D. A. *et al.* Anatomy of Heinrich Layer 1 and its role in the last deglaciation. *Paleoceanography* **32**, 284–303 (2017).

14. Bard, E., Rostek, F., Turon, J.-L. & Gendreau, S. Hydrological Impact of Heinrich Events in the Subtropical Northeast Atlantic. *Science* **289**, 1321–1324 (2000).

15. Bard, E., Hamelin, B. ,. Arnold, M. ,. Montaggioni, L. ,. Cabioch, G. ,. Faure, G. ,. Rougerie, F. Deglacial sa-level record from Tahiti corals and the timing of global meltwater discharge. *Nature* **382**, 241–244 (1996).

16. Lambeck, K., Rouby, H., Purcell, A., Sun, Y. & Sambridge, M. Sea level and global ice volumes from the Last Glacial Maximum to the Holocene. *Proceedings of the National Academy of Sciences* **111**, 15296–15303 (2014).

17. McManus, J. F., Francois, R., Gherardi, J.-M., Keigwin, L. D. & Brown-Leger, S. Collapse and rapid resumption of Atlantic meridional circulation linked to deglacial climate changes. *Nature* **428**, 834–837 (2004).

18. Vidal, L. *et al.* Evidence for changes in the North Atlantic Deep Water linked to meltwater surges during the Heinrich events. *Earth and Planetary Science Letters* **146**, 13–27 (1997).

19. Cruz, F. W. *et al.* Orbitally driven east–west antiphasing of South American precipitation. *Nature Geoscience* **2**, 210–214 (2009).

20. Stager, J. C., Ryves, D. B., Chase, B. M. & Pausata, F. S. R. Catastrophic Drought in the Afro-Asian Monsoon Region During Heinrich Event 1. *Science* **331**, 1299–1302 (2011).

21. Timmermann, A. *et al.* The influence of a weakening of the Atlantic meridional overturning circulation on ENSO. *Journal of Climate* **20**, 4899–4919 (2007).

22. Williamson, M. S. *et al.* Effect of AMOC collapse on ENSO in a high resolution general circulation model. *Climate Dynamics* **50**, 2537–2552 (2018).

23. Sadekov, A. Y. *et al.* Palaeoclimate reconstructions reveal a strong link between El Nino-Southern Oscillation and Tropical Pacific mean state. *Nat Commun* **4**, 255–258 (2013).

24. Koutavas, A. & Joanides, S. El Niño–Southern Oscillation extrema in the Holocene and Last Glacial Maximum. *Paleoceanography* **27**, (2012).

25. Thirumalai, K., Partin, J. W., Jackson, C. S. & Quinn, T. M. Statistical constraints on El Niño Southern Oscillation reconstructions using individual foraminifera: A sensitivity analysis. *Paleoceanography* **28**, 401–412 (2013).

26. Glaubke, R. H. *et al.* An Inconsistent ENSO Response to Northern Hemisphere Stadials Over the Last Deglaciation. *Geophysical Research Letters* **51**, e2023GL107634 (2024).

27. Wittenberg, A. T. Are historical records sufficient to constrain ENSO simulations? *Geophysical Research Letters* **36**, L12702 (2009).

28. Carré, M. *et al.* High-resolution marine data and transient simulations support orbital forcing of ENSO amplitude since the mid-Holocene. *Quaternary Science Reviews* **268**, 107125 (2021).

29. Rein, B. *et al.* El Niño variability off Peru during the last 20,000 years. *Paleoceanography* **20**, 10.1029/2004PA001099 (2005).

30. Briceño-Zuluaga, F. J. *et al.* Terrigenous material supply to the Peruvian central\hack\newline continental shelf (Pisco, 14\degree\,S) during the last 1000 years:\hack\newline paleoclimatic implications. *Climate of the Past* **12**, 787–798 (2016).

31. Yseki, M. *et al.* Millennial variability of terrigenous transport to the central–southern Peruvian margin during the last deglaciation (18–13\,kyr\,BP). *Climate of the Past* **18**, 2255–2269 (2022).

32. Sifeddine, A. *et al.* Laminated sediments from the central Peruvian continental slope: A 500 year record of upwelling system productivity, terrestrial runoff and redox conditions. *Progress in Oceanography* **79**, 190–197 (2008).

33. Stiles, C. A., Mora, C. I. & Driese, S. G. Pedogenic processes and domain boundaries in a Vertisol climosequence: evidence from titanium and zirconium distribution and morphology. *Geoderma* **116**, 279–299 (2003).

34. Taboada, T., Cortizas, A. M., García, C. & García-Rodeja, E. Particle-size fractionation of titanium and zirconium during weathering and pedogenesis of granitic rocks in NW Spain. *Geoderma* **131**, 218–236 (2006).

35. Stuut, J.-B. W. & Lamy, F. Climate variability at the southern boundaries of the Namib (southwestern Africa) and Atacama (northern Chile) coastal deserts during the last 120,000 yr. *Quaternary Research* **62**, 301–309 (2004).

36. Stuut, J.-B. W., Temmesfeld, F. & De Deckker, P. A 550 ka record of aeolian activity near North West Cape, Australia: inferences from grain-size distributions and bulk chemistry of SE Indian Ocean deep-sea sediments. *Quaternary Science Reviews* **83**, 83–94 (2014).

37. Mollier-Vogel, E., Leduc, G., Böschen, T., Martinez, P. & Schneider, R. R. Rainfall response to orbital and millennial forcing in northern Peru over the last 18 ka. *Quaternary Science Reviews* **76**, 29–38 (2013).

38. Gutiérrez, D. *et al.* Rapid reorganization in ocean biogeochemistry off Peru towards the end of the Little Ice Age. *Biogeosciences* **6**, 835–848 (2009).

39. Martin, L. C. P. *et al.* Lake Tauca highstand (Heinrich Stadial 1a) driven by a southward shift of the Bolivian High. *Science Advances* **4**, eaar2514 (2018).

40. Fornace, K. L. *et al.* A 60,000-year record of hydrologic variability in the Central Andes from the hydrogen isotopic composition of leaf waxes in Lake Titicaca sediments. *Earth and Planetary Science Letters* **408**, 263–271 (2014).

41. McGee, D., Donohoe, A., Marshall, J. & Ferreira, D. Changes in ITCZ location and cross-equatorial heat transport at the Last Glacial Maximum, Heinrich Stadial 1, and the mid-Holocene. *Earth and Planetary Science Letters* **390**, 69–79 (2014).

42. Takahashi, K., Montecinos, A., Goubanova, K. & Dewitte, B. ENSO regimes: Reinterpreting the canonical and Modoki El Niño. *Geophys. Res. Lett.* **38**, (2011).

43. Carré, M., Sachs, J. P., Schauer, A. J., Rodríguez, W. E. & Ramos, F. C. Reconstructing El Niño-Southern Oscillation activity and ocean temperature seasonality from short-lived marine mollusk shells from Peru. *Palaeogeography, Palaeoclimatology, Palaeoecology* **371**, 45–53 (2013).

44. Lagos, P., Silva, Y., Nickl, E. & Mosquera, K. El Niño-related precipitation variability in Peru. *Advances in Geosciences* **14**, 231–237 (2008).

45. Morera, S. B., Condom, T., Crave, A., Steer, P. & Guyot, J. L. The impact of extreme El Niño events on modern sediment transport along the western Peruvian Andes (1968–2012). *Scientific Reports* **7**, 11947 (2017).

46. Wells, L. E. Holocene history of the El Nino phenomenon as recorded in flood sediments of northern coastal Peru. *Geology* **18**, 1134–1137 (1990).

47. Keefer, D. K., Moseley, M. E. & deFrance, S. D. A 38,000-year record of floods and debris flows in the Ilo region of southern Peru and its relation to El Niño events and great earthquakes. *Palaeogeography, Palaeoclimatology, Palaeoecology* **194**, 41–77 (2003).

48. Rein, B. How do the 1982/83 and 1997/98 El Niños rank in a geological record from Peru? *Quaternary International* **161**, 56–66 (2007).

49. Carré, M. *et al.* Holocene history of ENSO variance and asymmetry in the eastern tropical Pacific. *Science* **345**, 1045–1048 (2014).

50. Garreaud, R., Vuille, M. & Clement, A. C. The climate of the Altiplano: observed current conditions and mechanisms of past changes. *Palaeogeography, Palaeoclimatology, Palaeoecology* **194**, 5–22 (2003).

51. Vuille, M., Bradley, R. S. & Keimig, F. Interannual climate variability in the Central Andes and its relation to tropical Pacific and Atlantic forcing. *J. Geophys. Res.* **105**, 12447–12460 (2000).

52. Cai, W. *et al.* Climate impacts of the El Niño–Southern Oscillation on South America. *Nature Reviews Earth & Environment* **1**, 215–231 (2020).

53. Espinoza-Morriberón, D. *et al.* Dynamics of Surface Chlorophyll and the Asymmetric Response of the High Productive Zone in the Peruvian Sea: Effects of El Niño and La Niña. *International Journal of Climatology* **45**, e8764 (2025).

54. Moy, C. M., Seltzer, G. O., Rodbell, D. T. & Anderson, D. M. Variability of El Niño/Southern Oscillation activity at millenial timescales during the Holocene epoch. *Nature* **420**, 162–165 (2002).

55. Zhang, Z., Leduc, G. & Sachs, J. P. El Niño evolution during the Holocene revealed by a biomarker rain gauge in the Galápagos Islands. *Earth and Planetary Science Letters* **404**, 420–434 (2014).

56. Cobb, K. M. *et al.* Highly Variable El Niño-Southern Oscillation Throughout the Holocene. *Science* **339**, 67–70 (2013).

57. Rodgers, K. B. *et al.* Radiocarbon as a thermocline proxy for the eastern equatorial Pacific. *Geophysical Research Letters* **31**, L14314 (2004).

58. Vellinga, M. & Wood, R. A. Global Climatic Impacts of a Collapse of the Atlantic Thermohaline Circulation. *Climatic Change* **54**, 251–267 (2002).

59. Brendryen, J., Haflidason, H., Yokoyama, Y., Haaga, K. A. & Hannisdal, B. Eurasian Ice Sheet collapse was a major source of Meltwater Pulse 1A 14,600 years ago. *Nature Geoscience* **13**, 363–368 (2020).

60. Heinrich, H. Origin and Consequences of Cyclic Ice Rafting in the Northeast Atlantic Ocean During the Past 130,000 Years. *Quaternary Research* **29**, 142–152 (1988).

61. Wu, L., Li, C., Yang, C. & Xie, S.-P. Global Teleconnections in Response to a Shutdown of the Atlantic Meridional Overturning Circulation. *Journal of Climate* **21**, 3002–3019 (2008).

62. Zhang, R. & Delworth, T. L. Simulated tropical response to a substantial weakening of the Atlantic thermohaline circulation. *Journal of Climate* **18**, 1853–1860 (2005).

63. Merkel, U., Prange, M. & Schulz, M. ENSO variability and teleconnections during glacial climates. *Quaternary Science Reviews* **29**, 86–100 (2010).

64. Dong, B. & Sutton, R. T. Enhancement of ENSO variability by a weakened Atlantic thermohaline circulation in a coupled GCM. *Journal of Climate* **20**, 4920–4939 (2007).

65. Dokken, T. M. & Jansen, E. Rapid changes in the mechanism of ocean convection during the last glacial period. *Nature* **401**, 458–461 (1999).

66. Liu, Z. *et al.* Evolution and forcing mechanisms of El Nino over the past 21,000 years. *Nature* **515**, 550–553 (2014).

67. Kienast, S. S. *et al.* Near collapse of the meridional SST gradient in the eastern equatorial Pacific during Heinrich Stadial 1. *Paleoceanography* **28**, 663–674 (2013).

68. Emile-Geay, J. *et al.* Links between tropical Pacific seasonal, interannual and orbital variability during the Holocene. *Nature Geosci* **9**, 168–173 (2016).

69. Luan, Y., Braconnot, P., Yu, Y. & Zheng, W. Tropical Pacific mean state and ENSO changes: sensitivity to freshwater flux and remnant ice sheets at 9.5Â ka BP. *Climate Dynamics* 1–18 (2015) doi:10.1007/s00382-015-2467-7.

70. Kageyama, M. *et al.* Climatic impacts of fresh water hosing under Last Glacial Maximum conditions: a multi-model study. *Climate of the Past* **9**, 935–953 (2013).

71. DiNezio, P. N. *et al.* Tropical response to ocean circulation slowdown raises future drought risk. *Nature* **644**, 676–683 (2025).

72. Zahn, R. *et al.* Thermohaline instability in the North Atlantic during meltwater events: Stable isotope and ice-rafted detritus records from Core SO75-26KL, Portuguese Margin. *Paleoceanography* **12**, 696–710 (1997).

73. Clement, A. C., Seager, R. & Cane, M. A. Orbital controls on the El Niño/Southern Oscillation and the tropical climate. *Paleoceanography* **14**, 441–456 (1999).

74. Brown, J. R. *et al.* Comparison of past and future simulations of ENSO in CMIP5/PMIP3 and CMIP6/PMIP4 models. *Clim. Past* **16**, 1777–1805 (2020).

75. Braconnot, P., Luan, Y., Brewer, S. & Zheng, W. Impact of Earth's orbit and freshwater fluxes on Holocene climate mean seasonal cycle and ENSO characteristics. *Climate Dynamics* **38**, 1081–1092 (2012).

76. Cai, W. *et al.* Increasing frequency of extreme El Nino events due to greenhouse warming. *Nature Clim. Change* **4**, 111–116 (2014).

77. Cai, W. *et al.* Increased variability of eastern Pacific El NiÃ±o under greenhouse warming. *Nature* **564**, 201–206 (2018).

78. Callahan, C. W. *et al.* Robust decrease in El Niño/Southern Oscillation amplitude under long-term warming. *Nature Climate Change* **11**, 752–757 (2021).

79. McPhaden, M. J., Santoso, A. & Cai, W. *El Niño Southern Oscillation in a Changing Climate*. vol. 253 (John Wiley & Sons, 2020).

80. Rahmstorf, S. *et al.* Exceptional twentieth-century slowdown in Atlantic Ocean overturning circulation. *Nature Climate Change* **5**, 475–480 (2015).

81. Caesar, L., Rahmstorf, S., Robinson, A., Feulner, G. & Saba, V. Observed fingerprint of a weakening Atlantic Ocean overturning circulation. *Nature* **556**, 191–196 (2018).

82. Yang, Q. *et al.* Recent increases in Arctic freshwater flux affects Labrador Sea convection and Atlantic overturning circulation. *Nature Communications* **7**, 10525 (2016).

83. Bevis, M. *et al.* Accelerating changes in ice mass within Greenland, and the ice sheet's sensitivity to atmospheric forcing. *Proceedings of the National Academy of Sciences* **116**, 1934–1939 (2019).

84. Weijer, W., Cheng, W., Garuba, O. A., Hu, A. & Nadiga, B. T. CMIP6 Models Predict Significant 21st Century Decline of the Atlantic Meridional Overturning Circulation. *Geophysical Research Letters* **47**, e2019GL086075 (2020).

85. Hassan, T., Allen, R. J., Liu, W. & Randles, C. A. Anthropogenic aerosol forcing of the Atlantic meridional overturning circulation and the associated mechanisms in CMIP6 models. *Atmospheric Chemistry and Physics* **21**, 5821–5846 (2021).

86. Ma, Q. *et al.* Revisiting climate impacts of an AMOC slowdown: dependence on freshwater locations in the North Atlantic. *Science Advances* **10**, eadr3243.

87. Aybar, C. *et al.* Construction of a high-resolution gridded rainfall dataset for Peru from 1981 to the present day. *Hydrological Sciences Journal* **65**, 770–785 (2020).

88. Huang, B. *et al.* Extended Reconstructed Sea Surface Temperature, Version 5 (ERSSTv5): Upgrades, Validations, and Intercomparisons. *Journal of Climate* **30**, 8179–8205 (2017).

89. Berger, A. Long-term variations of caloric insolation resulting from the earth's orbital elements. *Quaternary Research* **9**, 139–167 (1978).

90. Ng, H. C. *et al.* Coherent deglacial changes in western Atlantic Ocean circulation. *Nature Communications* **9**, 2947 (2018).

91. Salvatteci, R. *et al.* Centennial to millennial-scale changes in oxygenation and productivity in the Eastern Tropical South Pacific during the last 25,000 years. *Quaternary Science Reviews* **131, Part A**, 102–117 (2016).

92. Salvatteci, R., Schneider, R. R., Blanz, T. & Mollier-Vogel, E. Deglacial to Holocene Ocean Temperatures in the Humboldt Current System as Indicated by Alkenone Paleothermometry. *Geophysical Research Letters* **46**, 281–292 (2019).

93. Brodie, I. & Kemp, A. E. S. Variation in biogenic and detrital fluxes and formation of laminae in late Quaternary sediments from the Peruvian coastal upwelling zone. *Marine Geology* **116**, 385–398 (1994).

94. Heaton, T. J. *et al.* Marine20—The Marine Radiocarbon Age Calibration Curve (0–55,000 cal BP). *Radiocarbon* **62**, 779–820 (2020).

95. Ortlieb, L., Vargas, G. & Saliège, J.-F. Marine radiocarbon reservoir effect along the northern Chile-southern Peru coast (14-24°S) throughout the Holocene. *Quaternary Research* **75**, 91–103 (2011).

96. Carré, M., Jackson, D., Maldonado, A., Chase, B. M. & Sachs, J. P. Variability of 14C reservoir age and air-sea flux of CO2 in the Peru-Chile upwelling region during the past 12,000 years. *Quaternary Research* **85**, 87–93 (2016).

97. Blaauw, M. & Christen, J. A. Flexible paleoclimate age-depth models using an autoregressive gamma process. *Bayesian Analysis* **6**, 457–474 (2011).

98. Reinhardt, L. *et al.* High-resolution sediment echosounding off Peru: Late Quaternary depositional sequences and sedimentary structures of a current-dominated shelf. *Marine Geophysical Researches* **23**, 335–351 (2002).

99. Salvatteci, R. *et al.* Cross-stratigraphies from a seismically active mud lens off Peru indicate horizontal extensions of laminae, missing sequences, and a need for multiple cores for high resolution records. *Marine Geology* **357**, 72–89 (2014).

100. Weltje, G. J. & Tjallingii, R. Calibration of XRF core scanners for quantitative geochemical logging of sediment cores: Theory and application. *Earth and Planetary Science Letters* **274**, 423–438 (2008).

101. Bertrand, S. *et al.* Inorganic geochemistry of lake sediments: A review of analytical techniques and guidelines for data interpretation. *Earth-Science Reviews* **249**, 104639 (2024).

102. Saukel, C., Lamy, F., Stuut, J.-B. W., Tiedemann, R. & Vogt, C. Distribution and provenance of wind-blown SE Pacific surface sediments. *Marine Geology* **280**, 130–142 (2011).

103. Hill, I. G., Worden, R. H. & Meighan, I. G. Yttrium: The immobility-mobility transition during basaltic weathering. *Geology* **28**, 923–926 (2000).

104. Bern, C. R., Thompson, A. & Chadwick, O. A. Quantification of colloidal and aqueous element transfer in soils: The dual-phase mass balance model. *Geochimica et Cosmochimica Acta* **151**, 1–18 (2015).

105. Labille, J., Harns, C., Bottero, J.-Y. & Brant, J. Heteroaggregation of Titanium Dioxide Nanoparticles with Natural Clay Colloids. *Environ. Sci. Technol.* **49**, 6608–6616 (2015).

106. Velazco, F. *et al.* Flujos de material particulado y formación de una lámina de sedimentos en la plataforma continental interna frente al Callao durante El Niño Costero 2017. *Boletin Instituto del Mar del Perú* **36**, 428–451 (2022).

107. Du, X. *et al.* High-resolution interannual precipitation reconstruction of Southern California: Implications for Holocene ENSO evolution. *Earth and Planetary Science Letters* **554**, 116670 (2021).

108. Capotondi, A. *et al.* Understanding ENSO Diversity. *Bulletin of the American Meteorological Society* **96**, 921–938 (2015).

109. Sanabria, J. *et al.* Rainfall along the coast of Peru during strong El Niño events. *International Journal of Climatology* **38**, 1737–1747 (2018).

110. Aceituno, P. On the functioning of the southern oscillation in the South American sector. Part I: Surface climate. *Monthly Weather Review* **116**, 505–524 (1988).

111. Garreaud, R. & Aceituno, P. Interannual Rainfall Variability over the South American Altiplano. *Journal of Climate* **14**, 2779–2789 (2012).

112. Huerta, A. & Lavado-Casimiro, W. Trends and variability of precipitation extremes in the Peruvian Altiplano (1971–2013). *International Journal of Climatology* **41**, 513–528 (2021).

113. Takahashi, K. & Martínez, A. G. The very strong coastal El Niño in 1925 in the far-eastern Pacific. *Climate Dynamics* **52**, 7389–7415 (2019).

114. Echevin, V. *et al.* Forcings and Evolution of the 2017 Coastal El Niño Off Northern Peru and Ecuador. *Frontiers in Marine Science* **5**, 367 (2018).

115. Peng, Q., Xie, S.-P., Passalacqua, G. A., Miyamoto, A. & Deser, C. The 2023 extreme coastal El Niño: Atmospheric and air-sea coupling mechanisms. *Science Advances* **10**, eadk8646 (2024).

116. Hu, Z.-Z., Huang, B., Zhu, J., Kumar, A. & McPhaden, M. J. On the variety of coastal El Niño events. *Climate Dynamics* **52**, 7537–7552 (2019).

117. Quispe-Ccalluari, C. *et al.* An index of coastal thermal effects of El Niño Southern Oscillation on the Peruvian Upwelling Ecosystem. *International Journal of Climatology* **38**, 3191–3201 (2018).

118. Huyer, A., Smith, R. L. & Paluszkiewicz, T. Coastal upwelling off Peru during normal and El Niño times, 1981-1984. *Journal of Geophysical Research* **92**, 14,297-14,307 (1987).

119. Chamorro, A. *et al.* Mechanisms of the intensification of the upwelling-favorable winds during El Niño 1997–1998 in the Peruvian upwelling system. *Climate Dynamics* **51**, 3717–3733 (2018).

120. Fontugne, M., Carré, M., Bentaleb, I., Julien, M. & Lavallée, D. Radiocarbon reservoir age variations in the south Peruvian upwelling during the Holocene. *Radiocarbon* **46**, 531–537 (2004).

121. Barber, R. T. & Chavez, F. P. Biological consequences of El Niño. *Science* **222**, 1203–1210 (1983).

122. Espinoza-Morriberón, D. *et al.* Impacts of El Niño events on the Peruvian upwelling system productivity. *Journal of Geophysical Research: Oceans* **122**, (2007).

FIGURE 1

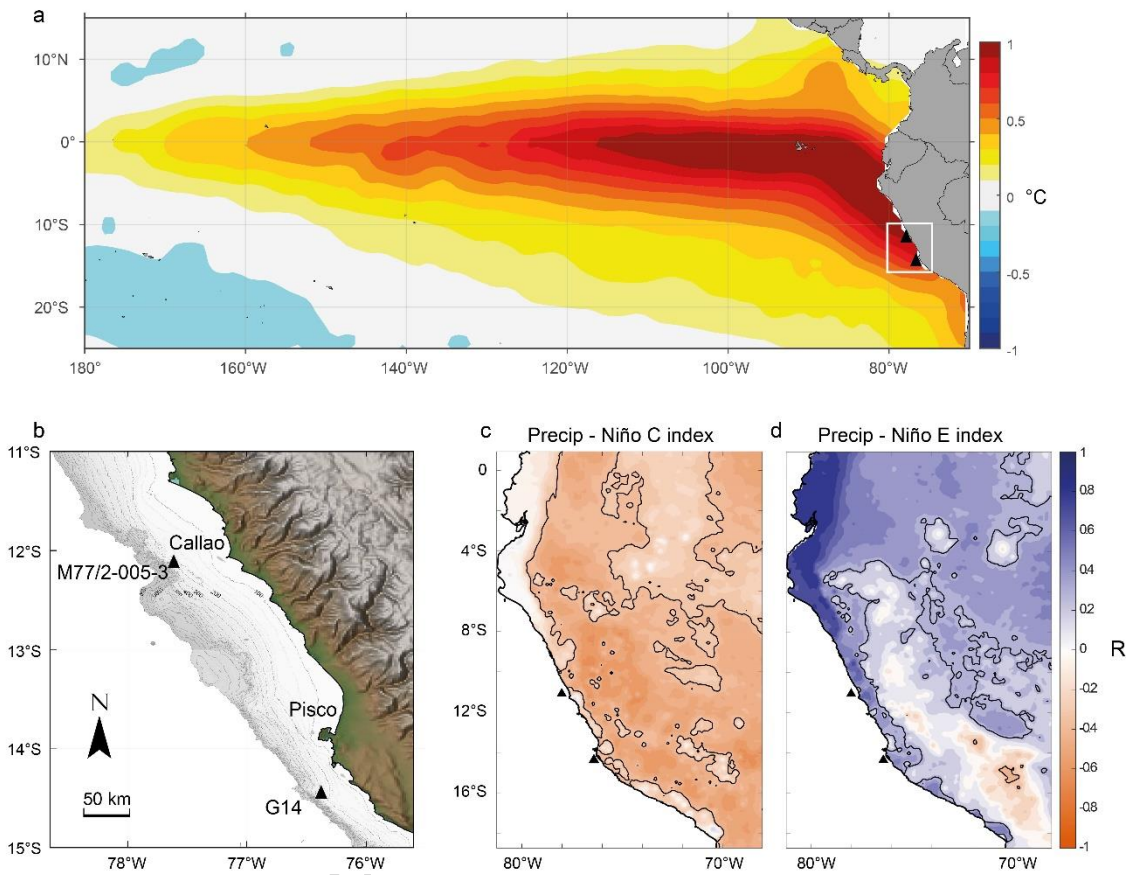

Figure 1. Study area. (a) Standard deviation of the Eastern Pacific ENSO E index (shading). The cores' locations (black triangle) and the study area (white box) enlarged in panel b are indicated. (b) Map of central Peruvian coast with the location of sediment cores M77/2-005-3 (Callao) and G14 (Pisco) in the Peruvian margin. (c) Pearson correlation coefficient between JFM rainfall in Peru (PISCO dataset, 0.1°, 1981-2019[87]) and the El Niño Central Pacific C index[42] calculated from ERSST5[88]). (d) Same for El Niño Eastern Pacific E index.

FIGURE 2

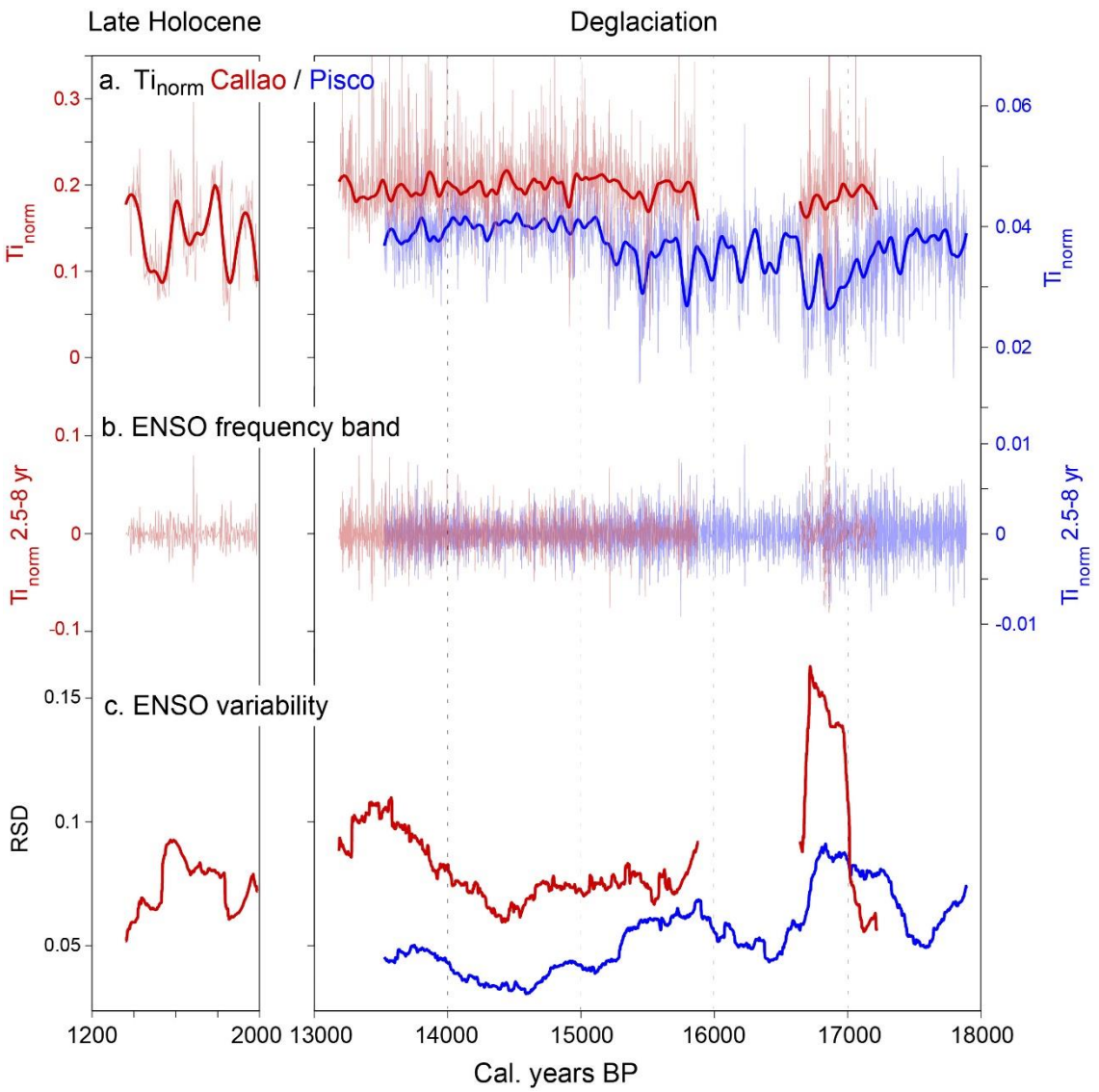

Figure 2. Titanium record of ENSO-related interannual climate variability in Peru. **a**, Normalized Ti counts in the M77/2-005-3 core off Callao (red) and in the G14 core off Pisco (blue). **b**, 2.5–8 year bandpass filtered record typical of ENSO variability. **c**, Variations of ENSO-related climate variability estimated by the relative standard deviation of the Ti_{norm} ENSO band over a 300-year moving window. Because of distinct sedimentary and analytical settings, the Pisco and Callao Ti records are represented on different scales.

FIGURE 3

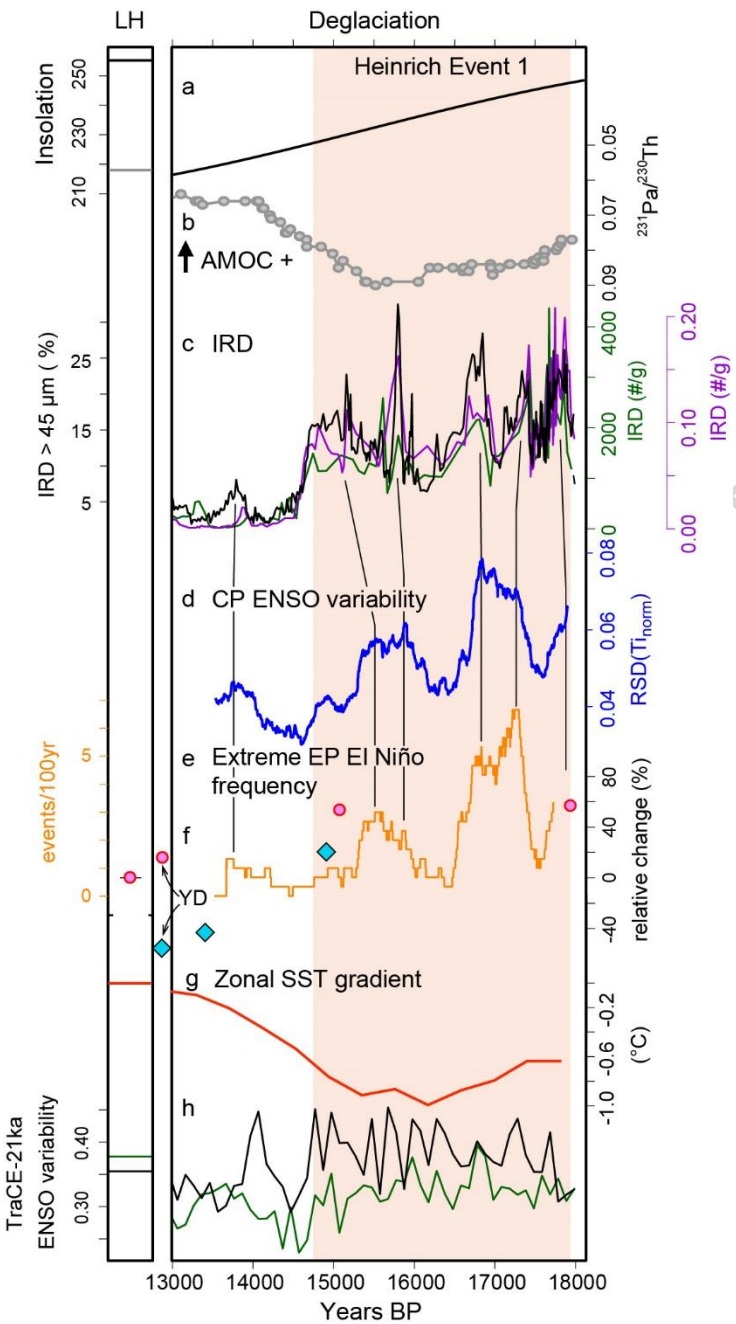

Figure 3. Deglacial ENSO millennial variability compared to North Atlantic records. The left narrow panel shows Late Holocene mean values (0-3ka). **a**, Seasonal insolation contrast (DJF-JJA) at 30°S[89]. **b**, Composite record of ^{231}Pa/^{230}Th in marine sediment reflecting AMOC

intensity[90]. **c**, Records of ice raft debris (IRD) flux in Norvegian sea cores MD95-2010 (green), GS07-148-17GC (black) and GIK23074 (blue)[59]. **d**, CP ENSO variability off Pisco over a 300-yr running window (blue) without extreme El Niño events. **e**, Frequency of extreme EP El Niño events per century off Pisco (orange). A tentative correlation aligning IRD peaks with ENSO maxima is proposed (black lines). **f**, foraminifera-based ENSO variability relative change in the eastern equatorial Pacific in core CD38-17P (pink dots)[23] and core MV1014-02-17JC (green diamonds)[26]. **g**, Pacific SST zonal gradient (red line)[23], and **h**, ENSO variability in CCSM3 TraCE-21k simulations with meltwater forcing only (black), and all forcings (green)[66].

Editor Summary:
El Niño–Southern Oscillation variability was not only stronger during the deglaciation but also correlated with North Atlantic records of iceberg discharge, according to analysis of finely laminated sediments from the Peruvian margin.

Peer Review Information:
Communications Earth and Environment thanks the anonymous reviewers for their contribution to the peer review of this work. Primary Handling Editors: Kyung-Sook Yun, Alireza Bahadori and Aliénor Lavergne. A peer review file is available.